Characterizing W sources in the all-W wall, all-RF WEST tokamak environment

C C Klepper, E A Unterberg, Y Marandet, D Curreli, A Grosjean, J H Harris, C A Johnson, A Gallo, M Goniche, Ch Guillemaut, et al.

Characterizing W sources in the all-W wall, all-RF WEST tokamak environment[†,‡]

C.C. Klepper[1], E.A. Unterberg[1], Y. Marandet[2], D. Curreli[3], A. Grosjean[4], J.H. Harris[1], C.A. Johnson[1], A. Gallo[5], M. Goniche[5], Ch. Guillemaut[5], J.P. Gunn[5], M. Raghunathan[2], E. Tsitrone[5], G. Ciraolo[5], L. Colas[5], D. Donovan[4], A. Ekedahl[5], D. Easley[4], G. Urbanczyk[5,&] and the WEST Team[¥]

[1]Oak Ridge National Laboratory, Oak Ridge, TN 37831, USA
[2]Aix Marseille Univ, CNRS, PIIM, UMR 7345, Marseille F-13397, France
[3]Nuclear, Plasma, and Radiological Engineering, University of Illinois at Urbana, Champaign, Urbana, IL 61801, USA
[4]Department of Nuclear Engineering, University of Tennessee, Knoxville, Tennessee 37996, USA
[5]CEA, IRFM, F-13108 Saint Paul Lez Durance, France
[¥]http://irfm.cea.fr/en/west/WESTteam/

E-mail: kleppercc@ornl.gov

Received xxxxxx
Accepted for publication xxxxxx
Published xxxxxx

Abstract

Experimental data, together with interpretive modeling tools, are examined to study trends in the tungsten (W) source in the all-W environment of the WEST tokamak, both from the divertor and from the main chamber. In particular, a poloidal limiter protecting an Ion Cyclotron Resonance Heating (ICRH) antenna is used as proxy for main chamber sourcing. The key study is carried out by stepping up Lower Hybrid Current Drive (LHCD) power, as the only auxiliary power source. Limiter and divertor W sources exhibit a qualitatively similar proportionality to the total power crossing the separatrix, P_{SEP}, although the main chamber source remains substantially lower than the divertor source, for the range of P_{SEP} accessible in the experiments. Intepretive modeling of the limiter source is carried out with a Particle-in-Cell (PIC) sheath model coupled to a surface sputtering model. Oxygen is used as proxy for all light impurity species allowing for characterization of the critical W erosion regions. To get a good quantitative match to the data, it is necessary to assume that the oxygen arrives at the surface mostly at high ionization stages (4+ and above). A separate simulation with SOLEDGE-EIRENE, constrained to measured upstream scrape-off-layer plasma profiles, gives oxygen fractional abundances that are compatible with the PIC simulation result. This is understood to arise from transport processes that dominate over recombination. Substituting the LHCD by ICRH, in an equivalent experiment, the local W source exhibits a x3 enhancement. This can be matched by the simulation, by assuming local RF electric field rectification, based on ~100eV peak-to-peak, near-antennna electric field. This work has highlighted the particular importance of understanding the ion charge state balance of light impurities as these are most likely the dominant sputtering species in fusion devices with high-Z walls.

Keywords: edge plasma modelling, light impurity transport, WEST, plasma sheath, tungsten erosion

[†]Based on an Invited Talk, 47th European Physical Society Conference on Plasma Physics, 21-25 June 2021, Sitges, Spain.

[&]Presently with Institute of Plasma Physics, Chinese Academy of Sciences, Hefei, Anhui 230031, China

1. Introduction

In a magnetically confined fusion energy device with high-Z metallic plasma facing surfaces, it is important to evaluate material surface sources to the plasma for two reasons: (i) unmitigated plasma contamination of the core plasma by high-Z imputities can be detrimental to energy confinement and this effect can already critically impact plasma performance even in short pulse plasmas, and; (ii) the plasma-surface interactions that generate these sources can impact the lifetime of plasma-facing components (PFC), as well as lead to material migration with related reactor maintenance challenges. Ultimately, predictive capability for PFC net erosion is needed as this drives the impurity sourcing and component lifetime issues called out above. This capability is a critical task for this area of fusion energy science, and this paper is an initial attempt, albeit limited in scope, at developing predictive capabilities.

Tungsten (W) is currently the choice material for the ITER divertor [**1**]. As a result, the most significant studies of W sources under ITER and next generation, reactor-relevant conditions have been for the divertor region of current devices, including ASDEX-U and JET ITER-like Wall [**2, 3, 4**, **5**].

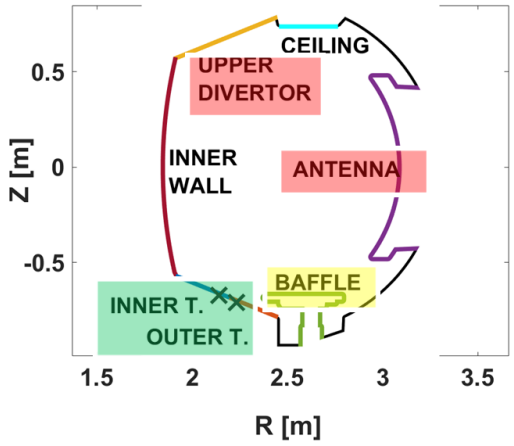

Figure 1. Illustration of the WEST plasma-facing surface regions. Main chamber regions that are weakly screened are highlighted in red, compared to the highly screened divertor regions (green).

The WEST tokamak, featuring all W plasma facing components [**6**], provides the opportunity to study W sources from both the divertor and the main chamber in a systematic way. Furthermore, with long-pulse capability as part of its design (up to 1000 secs plasma shots envisioned for its upcoming fully actively cooled divertor phase), WEST also provides the further opportunity to extend the studies to long-pulse tokamak operation, where real-time surface evolution and material migration can impact the sources from both the divertor and the main chamber.

In diverted configuration tokamak discharges, main chamber components are typically separated from the core plasma by a significant gap, and one would anticipate less impurity production from main chamber surfaces. Hence, the significance of these main chamber sources on core contamination can be underestimated. In particular, the core W contamination can be greatly enhanced due to less screening at main chamber locations, where a lower plasma density results in increased ionization mean free path length compared to the divertor [**7, 8, 9**]. This is illustrated in Fig. 1.

When extrapolating to fusion reactor timescales, one could show that the net material generated from erosion of an all- W wall can increase by orders of magnitude. For instance, in Ref [**10**] wall erosion due to charge exchange (CX) neutrals is predicted to increase by two orders of magnitude when scaling up from current devices to ITER and another two orders of magnitude from ITER to a typical fusion demonstration reactor (e.g. CFETR). Although that study only accounted for erosion due to CX neutrals, which affect any wall surface, independent of magnetic field connection, our present study shows that highly charge impurities can dominate the process at the main chamber plasma-facing surfaces, such as limiters and actuators, and provides a baseline for how the erosion at these surfaces could scale up

This paper focuses on the interpetation of experimental data from a set of WEST plasma discharges specifically intended to systematically explore sources of W arising from and beyond the divertor, and how these scale with discharge characteristics, such as the input power. These studies were carried out to validate codes in preparation for long-pulse capability with a fully actively cooled lower divertor (*WEST Phase 2*). A subset of such computational tools are explored and applied specifically to interpret observed characteristics of the W sources, at limiter locations that are optimally accessed with visible spectroscopy used for *in-situ* erosion measurements. The latter is a key diagnostic for the characterization of plasma edge impurities and a diagnostic that has been realised through significant development, overcoming the enormous optical access limitations imposed by cryostat-clad toroidal fusion energy devices [**11**, **12**].

In the remainder of this Section, we briefly expand on the relevant diagnostic capability on WEST. This is then followed by an overview of the set of experimental observations, together with a brief description of the emerging modeling workflows and how it is partially deployed for an interpretive study of the data at an outboard limiter, which is used as proxy for any main chamber region. In Section 2, the application of the computational tools, one set for the main chamber and one set for the divertor, are described, and the corresponding interpetive outcomes are presented.

1.1 Facility and measurement capabilities

A thorough description of the plasma facing components, including the accessing diagnostics available in WEST Phase 1, can be found in Ref [**13**]. For the divertor measurement, regions of the inner and outer lower divertor are accessible by visible spectroscopy sightlines (one fan of sightlines for the inner and one for the outer divertor). For the main chamber, a (poloidal, outer) lateral protection limiter is used, one of two such limiters bracketing one of the ion-cyclotron resonance heating (ICRH) antennas, specifically the one referred to as IC2R. The IC2R limiter is selected as the "main chamber proxy" in this work, because it had the best spectroscopic coverage and also because it was placed closest to the separatrix in the dedicated experimental studies and thus could be considered to be the primary impurity source from the outer main chamber.

1.2 Experiment design. Details of the data examined in the present study are shown in Figure 2. Here, two typical shots with a power scan in the LHCD power injection are performed, with LH as the only source of auxiliary power.

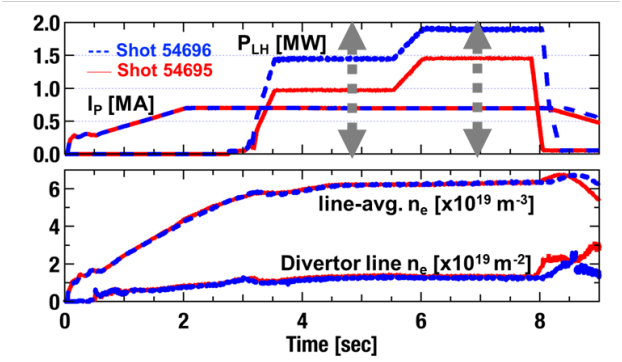

Figure 2. WEST discharge parameters used for this work., The vertical double-arrows illustrate the RCP plunges, one plunge per P_{LH} plateau.

Key elements of these experiments included: (i) steps in the LH power, P_{LH}, that were long enough to provide for good signal to noise in spectroscopic signal integration, a critical requirement for off-divertor source studies, as will be explained, and (ii) One plunge per such LH-power plateau of the reciprocating probe (RCP); described in Ref. [**14**]

The primary experiment is limited to LH heating-only because at the LH frequencies the RF wave rectification in the edge plasma does not occur. As such, RF-enhanced sheaths are not expected at the plasma facing surfaces of interest, including the guard (lateral protection) limiters of the various RF antennas.

1.3 Computational tools for the outboard limiter study

A computational model of the problem was constructed using tools from the US SciDAC-PSI workflow on Plasma-Surface Interactions [**15**]. In the present study, a limited subset of the workflow was used, including: (1) the hPIC [**16**] particle-in-cell code for the solution of the near-surface plasma and the determination of the energy-angle distributions of the ions impacting on the surfaces; and (2) the combined, binary-collision approximation (BCA) tools, F-TRIDYN and RustBCA [**17**, **18**], which addresses a variety of ion-surface interaction processes, such as ion implantation, reflection, and impurity sputtering. The latter, combined BCA tools, will be henceforth referred to simply as RustBCA. The workflow is designed such that the hPIC-RustBCA pair of codes can be interfaced with SOL codes such as SOLPS or UEDGE, for the determination of the plasma background in the Scrape-Off Layer (SOL). However, in this study, the input plasma are introduced directly from experimental measurements as projected to the common locations of interest in front of the IC2R outboard limiter.

2. Interpretive modelling studies

Two interpretive modeling studies are discussed in this Section. For the main chamber case, hPIC-RustBCA code pair, discussed in Section 1.3, is used to simulate the gross erosion process at the outbooard limiter surface. The plasma input to hPIC is taken directly from local, edge plasma measurement, not from plasma simulation, to keep the near-surface simulations in conditions as close as possible to the experimental conditions.

For the divertor data, including a significant inner-outer strike-region asymmetry, the SOLEDGE-EIRENE code [**19**] is deployed, with particular focus on understanding the role of light impurities using oxygen as a proxy impurity. This choice of proxy impurity is based on the idea that oxygen would likely be the dominant light impurity during the experimental campaign of the present study, when the use of boronization was still minimal. A key trend of interest in this interpretive study is the dependence of the observed in-out asymmetry in the measured, divertor neutral tungsten line emission (W I) on injected LH power. These SOLEDGE-EIRENE simulations are ultimately intended to fill in measurement gaps, e.g. the baffle erosion strength (as shown in Fig. 1), where spectroscopy signals were too low to draw useful conclusions, or on main chamber limiters, leveraging the extended grid capability of the code. In this work, we rather use the SOLEDGE-EIRENE simulations to complement the available experimental data on outboard limiters, in particular on impurities. Indeed, these simulations point towards the possibility that very high ionization states of oxygen may be dominating the W erosion process on the limiter in spite of the low electron temperature there. For this code comparison, SOLEDGE is constrained by the same upstream SOL conditions as the hPIC/RustBCA simulations, and iterations

are made between each code runs to determine the ionization balance in front of the limiter.

2.1 Key trends for modelling light impurities and W sources. The experimental setup has allowed the study of source trending at and away from the divertor as a function of one parameter at a time, such as the choice and power level of auxiliary heating. The W I 4009 Å, neutral W emission line, is commonly used as proxy for gross surface erosion (see, e.g., Ref.[**3**]). Although this is strongest spectral line for neutral W in the visible range of the spectrum, it is still relatively weak in OH or L-mode conditions (see, e.g., in Ref. [**20**]) which are apply to the experiments studied in this work. This becomes a particularly challenging issue for measurements of this spectral line at limiter surfaces, i.e., locations having a significant gap with the separatrix and thus in a region of much lower collisional excitation of this spectral line, and therefore long integration periods (~2sec) are performed. Additionally, some challenges in spectral fitting in this environment are discussed in Ref. [**21**].

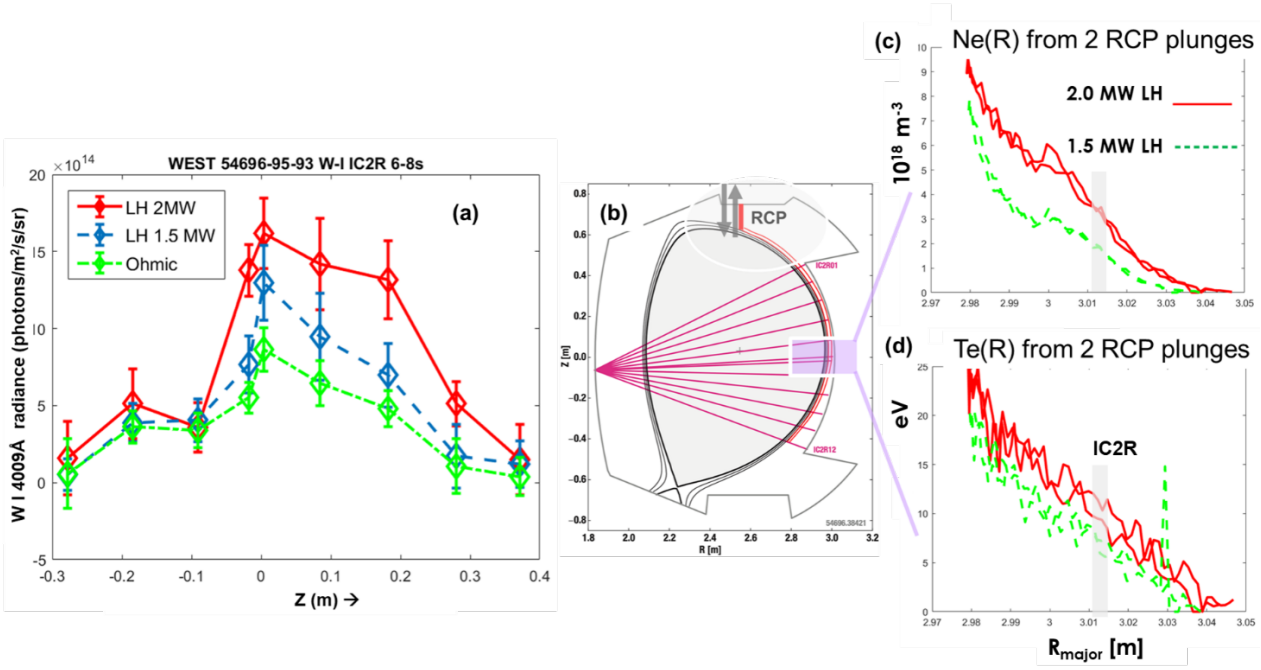

Figure 3. (a) Neutral W emission (W I 4009 Å) as a function of vertical position (Z) along the IC2R limiter. (b) WEST equilibrium for lower single-null (LSN)plasma with the relative location of the reciprocating probe (RCP) and of the visible spectrometer sightlines viewing the outboard limiter; the limiter is located on the low field side (LFS) where sightlines end. (c) and (d) SOL profiles from the RCP as projected on the midplane of n_e and T_e, respectively; the diffuse vertical lines indicate the approximate position of the limiter IC2R.

Fig. 3a shows clear trends in the neutral W emission with increasing power across the poloidal extent of the limiter, as a function of vertical position (Z) along the IC2R limiter, as illustrated in Fig. 3b, in which the sightlines are shown to span the entire poloidal extent of this limiter. The three datasets plotted in Fig. 3a result from spectral fitting performed after averaging the 6s to 8s plateau region (the second LH plateau region in Fig. 2) to optimally differentiate the impact of the input power over the spectral fitting error bars, as seen in Fig. 3a. These datasets come from the second plateau region of WEST shots 54695, 54696 of Fig. 2, with the Ohmic shot 54693 completing the set.

Fig. 4 shows the peak emission values from Fig. 3a as a function of P_{SEP}, the net power crossing the separatrix, and also as a function of SOL T_e. SOL T_e is from the RCP profile projection to the midplane (Fig. 3b,c) and with values read at ~2cm outside the separatrix. More precise values for the SOL plasma right at the limiter surface are determined in the limiter modelling study in Section 2.2.

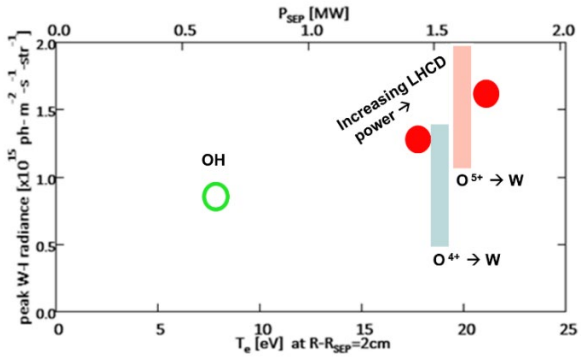

Figure 4. W I 4009 Å peak emission at the outer limiter as a function of P_{SEP} and of SOL T_e. The open green circle is the OH case, and the two filled red circles are the two LHCD-only cases (P_{LH} of 1.5 MW and 2 MW) as in Fig. 3. The vertical bars relate to the interpretive modelling study of Section 2.2.

It is noted that the significant poloidal variation in the W I emission along the limiter, as seen in Fig. 3, is due to geometric effects, i.e., in the relative shape of this actively cooled limiter and the radial position of its individual tiles with respect to the separatrix and to the open flux surfaces outside it. It is not power dependent.

In the case of the divertor, there is also a significant asymmetry (radial in this case) in W I peak emission, and this asymmetry is observed to be strongly dependent on P_{SEP} [**21**]. This is illustrated in Fig. 5, with the W I emission (Fig. 5a) plotted for the Ohmic case; also, for the highest power of the dedicated shots of Fig. 3 and 4; and, additionally, for an even higher power shot (54548, P_{SEP} ~2.3MW) with otherwise nearly same conditions as for the dedicated power scan. As also discussed in [**21**], although the intensity of other edge impurity species, with signature spectral lines in the same visible spectral-range, exhibit some in-out asymmetry, none are as significantly sensitive to P_{SEP}, as is the W I emission, nor show the saturation and drop at higher powers. It is important to remind that these are measured brightness values; conversion factors to fluxes will also depend on the local plasma parameters. For reference, also plotted in this Figure is the emission from three light impurity species (O, C and B, all in singly ionized state) with prominent spectral lines found near the W I 4009 Å line.

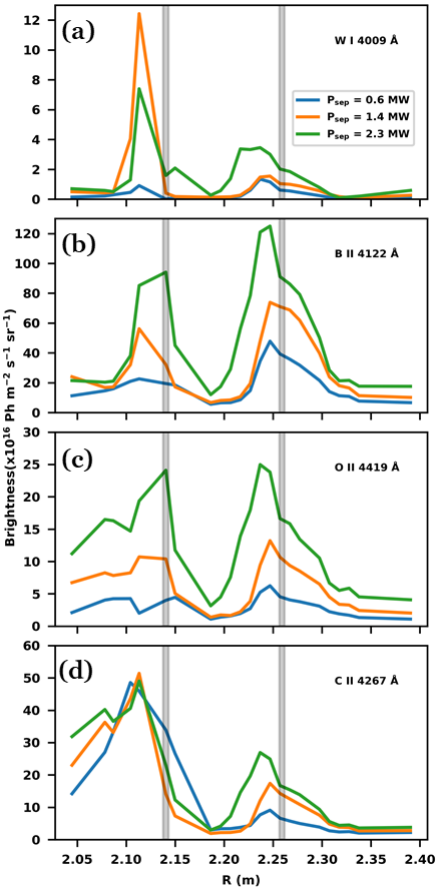

Figure 5. (a) Divertor W I profile asymmetry changes with with P_{SEP} . Subfigure (b – d) Corresponding spatial profiles of light impurity low ionization stages whose spectral lines are detectable in the same spectra with the W I 4009Å line.

2.2 Modelling study of the sources from the limiter.

In Fig. 3b the WEST equilibrium for the lower single-null discharges of this study is illustrated, together with the relative location of the RCP. Figures 3(c) and 3(d) show the local edge measurements from the RCP once projected on the midplane along the same magnetic flux tubes (red lines in Fig, 3b).

The density and temperature as a function of the vertical coordinate along the limiter is reported in Fig. 6 for the higher power case of Fig. 3c,d. These vertical profiles are produced by further projection of the mid-plane radial profiles from Fig. 3c,d, along magnetic flux surfaces, and then up to the corresponding limiter tile. As expected, both n_e and T_e have a peak at the midplane, where the outer limiter is closest to the LCFS. The vertical asymmetry on the profile is due mainly to the geometrical asymmetry of the upper vs. lower portion of the limiter, which have a different gap with respect to the LCFS.

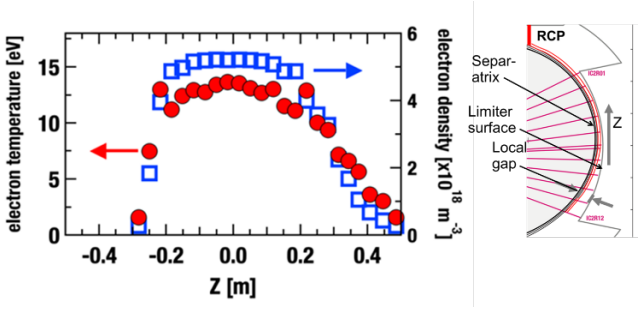

Figure 6. Plasma parameters at the outer limiter surface after projection along magnetic flux surfaces. Inset is zoomed in from Fig. 3b to illustrate the local limiter-separatrix gap dependence on Z.

The amount of sputtered tungsten was calculated using the coupled pair of codes hPIC – RustBCA, as defined in Section 3.1. The analysis was focused on determining the amount of neutral tungsten emitted at the poloidal locations observed by visible spectroscopy and on comparing the modeling results against the corresponding absolutely-calibrated spectral radiance values. The hPIC code was used to resolve the structure of the magnetic (Chodura) presheath at each point of observation, and to determine the energy-angle distributions (IEAD) of the ions impacting on the surfaces [**22**]. The IEADs were then used as an input in the RustBCA code for the determination of the W particle fluxes sputtered by the surfaces. The RustBCA model was run for a plasma atomic composition of 95% deuterium and 5% oxygen. Because of the low n_e, T_e conditions near the surface of the observed IC2R limiter (~mid-10^{18} m^{-3}, ~12 eV), this first simulation assumed all the impinging oxygen ions are singly ionized.

As expected, the deuterium population did not produce any detectable sputtering event, due to the low kinetic energy of the main plasma ions at the limiter. All tungsten sputtering was caused solely by the oxygen in the simulation. As reported in Fig. 7, the calculated particle fluxes at the outboard limiter depend on total input power (all LH power in this case). Figure 7a shows the results for two LH power levels of 1.5 and 2.0 MW, showing peak midplane fluxes of the order of $\Gamma_W = 10^{16}$ $m^{-2}s^{-1}$ and $\Gamma_W = 10^{17}$ $m^{-2}s^{-1}$, respectively. The simulations showed that sputtering of tungsten was caused by the high-energy tails of the distribution function of the oxygen ions having energy above the sputtering threshold. As an extra check of the model, we replot in Fig. 7b all the data of Fig. 7a, but this time versus Te, and we see that all the data effectively line-up on a single curve that is qualitatively similar to light impurity sputtering curves for W in the literature, e.g., as the carbon on W sputtering yield curve in Fig. 2 in Ref [**23**].

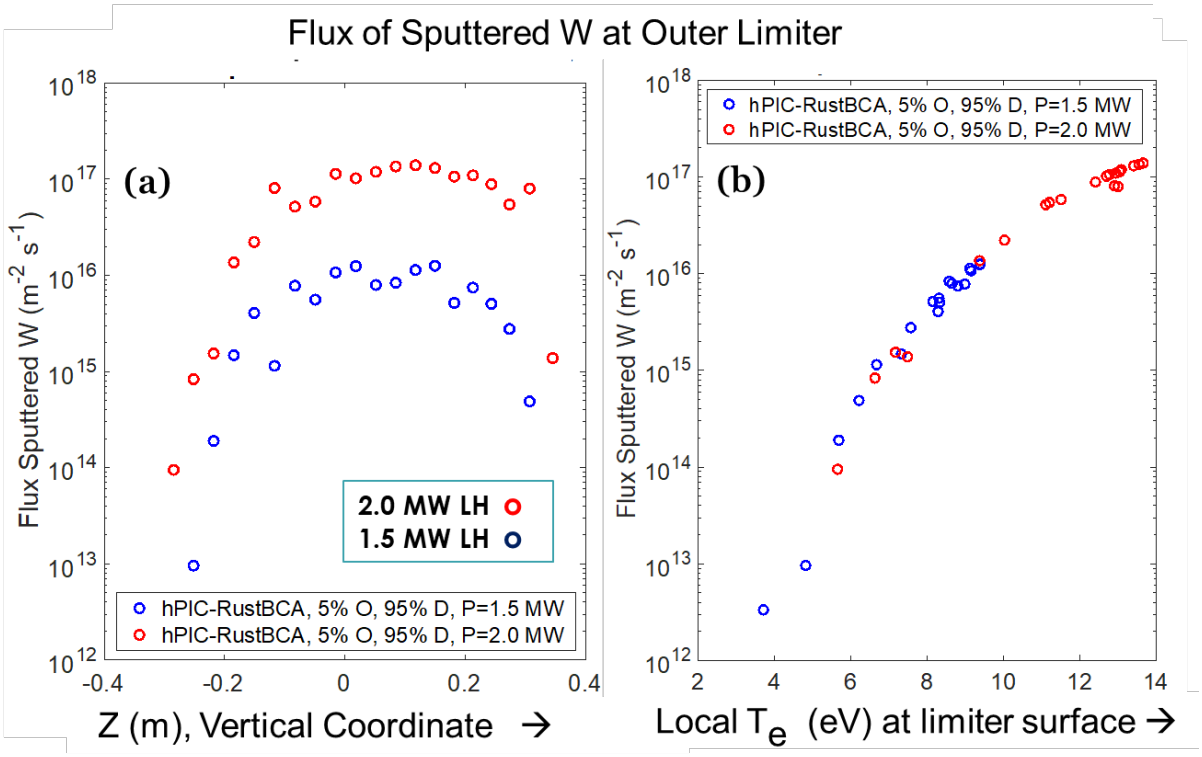

Figure 7. (a) Flux of sputtered W, as calculated from hPIC-RustBCA for the two P_{LH} levels; (b) Same data as in (a) but plotted as a function of the electron temperature of the plasma near the surface of the observed limiter (from Fig. 6)

In order to compare the results from the model against the measured spectral intensities, an equivalent spectral radiance was derived by multiplying the flux of sputtered tungsten Γ_W from the model by the the conversion factor, or inverse ionization efficiency, S/XB, specific to the W I 4009 Å line. There are large uncertainties associated with atomic calculations and collisional radiative model of neutral tungsten. Figure 8 shows the values of S/XB as a function of electron temperature, as determined from two different sources in literature [**24**, **25**] and one from a current study using the ColRadPy code [**26**].

The atomic rates used for the latter are the same as used in [**27**], the excitation rates come from a Dirac *R*-matrix electron impact excitation calculation preformed by [**28**] which included spin-changing collisional rates. Ionization rates for this analysis were calculated using the Exchange Classical Impact (ECIP) method [**29**]. These approximate rates account for much of the uncertainty in the S/XB. There is currently no non-perturbative ionization calculation for neutral tungsten. Recombination of W^{1+} was not considered as it is insignificant when compared to other rates for plasma boundary conditions.

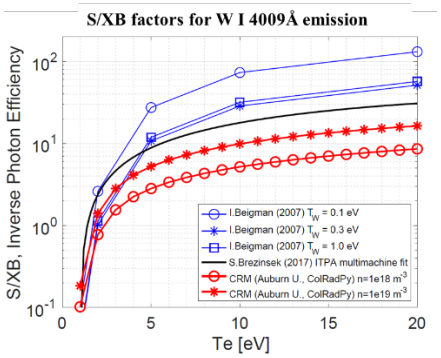

Figure 8. Inverse photon efficiencies from three sources.

.

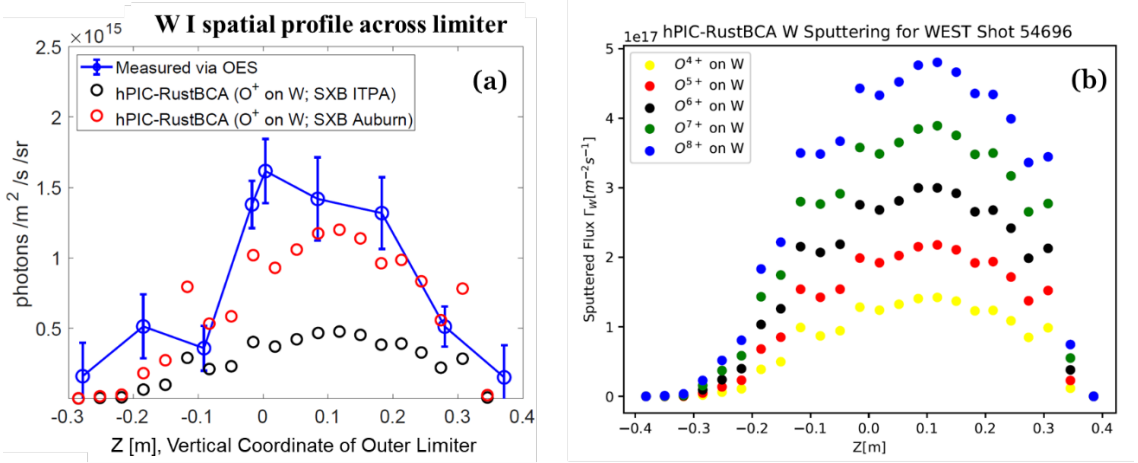

Figure 9. (a): Spatial profile of the W I 4009A line across the poloidal extent of the observed limiter. The error bars in the measurement are strictly from the certainty of the spectral line fit. Both parts of this hPIC-RustBCA simulation assume only singly ionized oxygen at 5% local concentration. (b): Study of sensitivity to oxygen ionization stage.

Figure 9a shows the result of applying these inverse ionization efficiencies to the higher power case (i.e. $P_{LH} = 2$ MW, or $P_{SEP} = \sim 1.7$ MW) of the first hPIC-RustBCA simulations that were shown in Fig. 7. The experimental radiance values provided for comparison are from Fig. 3a and for this same power case; the error bars from the spectral line fitting. It is important to recall that, for this simulation, the oxygen was taken to be 5% of the total ion density entering the presheath. Another assumption made was that, in the tenuous plasma near the antenna limiter, all the oxygen would be singly ionized. This assumption was of further interest, given that singly ionized stages of light impurities can be measured with visible range spectroscopy (as shown in Fig. 5) and thus could be potentially used to constain the simulations. However, it is seen in Fig. 9a that absolute values of simulated versus measured W I emission differ by up to 5x, especially when using the widely used ITPA S/XB factors.

Aside from uncertainty in the inverse photon efficiencies directly impacting the comparison to measured values, there are two major sources of uncertainty in the sputtering calculations performed with hPIC-RustBCA and these are related to: (1) the unknown impurity composition and impurity distribution within the discharge, and (2) the actual distribution of higher charge states (eg. O^{+}, O^{2+}, O^{3+}, etc.) resulting from the combined action of plasma transport and collisional-radiative processes. As in most tokamaks, the actual impurity composition (O, Cu, C, F, Si, etc.) and the relative concentration of these different impurities are known only up to a certain degree of accuracy. Some clues on the composition can be inferred from the line analysis of optical emission spectroscopy, but relative concentrations are unknown in most of the cases. In addition, the charge distribution for each impurity is also unknown, and difficult to infer without a radiative balance accounting for detailed transport effects and drifts. The charge distribution plays a role in the determination of W erosion, since atoms having different charge states (Z=1+, 2+, 3+,...) gain different energy when they pass across the sheath electric field. The present effort is not only attempting to better quantify these uncertainites, but it is also highlighting gaps in both measurement and modeling workflows in reducing the uncertainity.

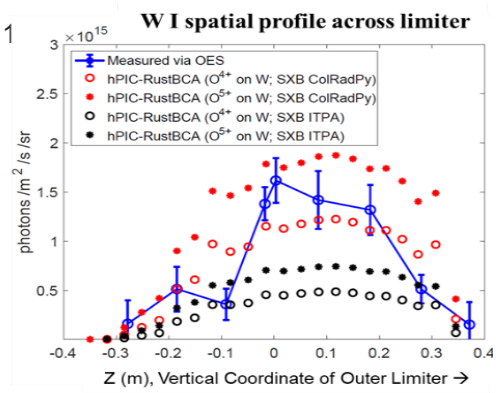

Figure 10. Same as Fig. 9a, except using higher ionization stages for oxygen.

In the present hPIC-RustBCA numerical simulations, oxygen is used as *light impurity proxy*, i.e. as the only light species different than deuterium, and thus available to contribute to the sputtering of W. In order to address the uncertainty related to the charge distribution, a sensitivity study was performed as a function of charge number from oxygen O^{4+} to fully-stripped O^{8+}, keeping the plasma composition fixed at 95% deuterium and 5% oxygen. Figure 9(b) reports the results of this sensitivity study, showing the expected range of sputtered flux Γ_W = 1-5 x 10^{17} #/m^2/s for charge states from O^{4+} to O^{8+}.

Of course, the inverse photon efficiency S/XB also plays an important role in overall uncertainty during the conversion of sputtering fluxes to absolute spectral radiance, as already discussed. However, it can be seen in Fig. 10 that a near quantitative match to the experimental data can be obtained by running hPIC-RustBCA for combination of O^{4+}, O^{5+} , esp. if the ColRadPy S/XB values are considered, and assuming a 5% concentration. This improved quantitative agreement and the range of uncertainty are also illustrated with the vertical bars in Fig. 4.

To get a better handle on which charge states of oxygen are most likely to be present at the limiter location, a time-dependent ionization balance was carried out (Fig. 11). The time-dependent ionization balance was completed using the collisional radiative code ColRadPy [**26**] with atomic data taken from the ADAS database [**29**] It is noted that there are no thermal charge exchange rates in the ADAS database for oxygen. The inclusion of thermal charge exchange would create another path for recombination and lead to a lower charge state distribution for a given time than what is shown in Fig. 11. Since oxygen is assumed to be one of the main sputtering ions in WEST plasmas, the calculation of these rates would be extremely valuable. It is further assumed that nearly all oxygen ions which end up at the limiter are coming from the confined plasma, not directly from the wall in the SOL, e.g. via recycling. Therefore, in this time-dependent ionization balance, all oxygen is started as fully ionized O^{8+}, recombining through the SOL until reaching the limiter. The time points along the absissae effectively represent time for the oxygen to reach the limiter from the separatrix.

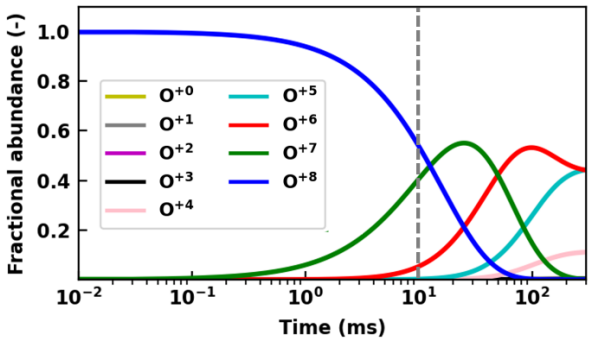

Figure 11. Time dependent ionization balance. The dashed line marks the 10 ms timescale, which the SOLEDGE-EIRENE simulation (Section 2.4) estimates for light impurity transport time across the SOL to the outer limiter.

The vertical dashed line in the Figure marks the 10 ms timescale, which is consistent with the particle transport coefficient, D, used later in SOLEDGE-EIRENE simulations to match upstream profiles (from an independent, parallel

study, see Section 2.4). The estimates for light impurity transport time for the distance, d, across the SOL to the outer limiter is obtained as ~ D/d^2. It is clear that for such short timescale, the charge state distribution is dominated by much higher states than even what was assumed in the simulation of Fig. 10. One would need to assume more than an order of magnitude higher transport times to get, e.g., O^{5+} to dominate. It is also noted that charge state distribution at 10 ms will depend significantly on the initial charge state of oxygen coming from the core plasma; the final distribution will be lower with a lower initial charge state. The distribution for τ >>10 ms is not altered as much by an initial lower charge, as such distribution would be close to equilibrium.

Although the precise charge distribution is not known, the outcome of this ionization equilibrium study is also clearly consistent with the idea that ionizations charges >> O^{1+} must dominate sputtering at the limiter. The message that this sends to the design of future experiments is that the measurement of the low ionization stages, which are straightforwardly accessible with the existing visible spectroscopy capability is not likely sufficient for improving model-to-experiment validation. Future experiments would need to assure availability of VUV data for boundary region light impurities (as used in Ref. [**30**]), and or access to near-UV range of visible spectroscopy hardware. An example of the latter can be found in [**3**] in which singly ionized W emission was accessed in this region, which is however inaccesible in WEST due to long (several 10s of meters) optical fiber cable used to transport the collected plasmal light emission to the visible spectrometers.

2.3 Modelling study at the limiter with ICRH-only

As mentioned, LH waves do not rectify in the edge plasma; however, ICRH waves are subject to this effect, leading to enhanced sheath potentials. Here analysis on ICRH-only discharges is completed mainly to illustrate the importance of this effect, which must be considered in an all-RF environment, as is WEST; also to provide a preliminary test of including an RF sheath feature in the hPIC-RustBCA pair of codes.

Figure 12 shows processing of shots from both the LH-only and ICRH-only sets, using the heuristic approach taken in [**31**, **32**] whereby the W I radiance values (Fig. 12b) are divided by the intensity a spectrally-near, deuterium Balmer-series line (D_ε, in this case) providing an effective yield (Fig. 12d). This is to illustrate the impact of the RF sheath on the sputtered flux, as a result of increased ion energies due to the increased effective sheath potential. Clearly the effect is highest for the shot with all the ICRH power applied to the observed antenna (WEST Shot 55741) consistent with the idea that the locally rectified sheath potential would be highest in this case.

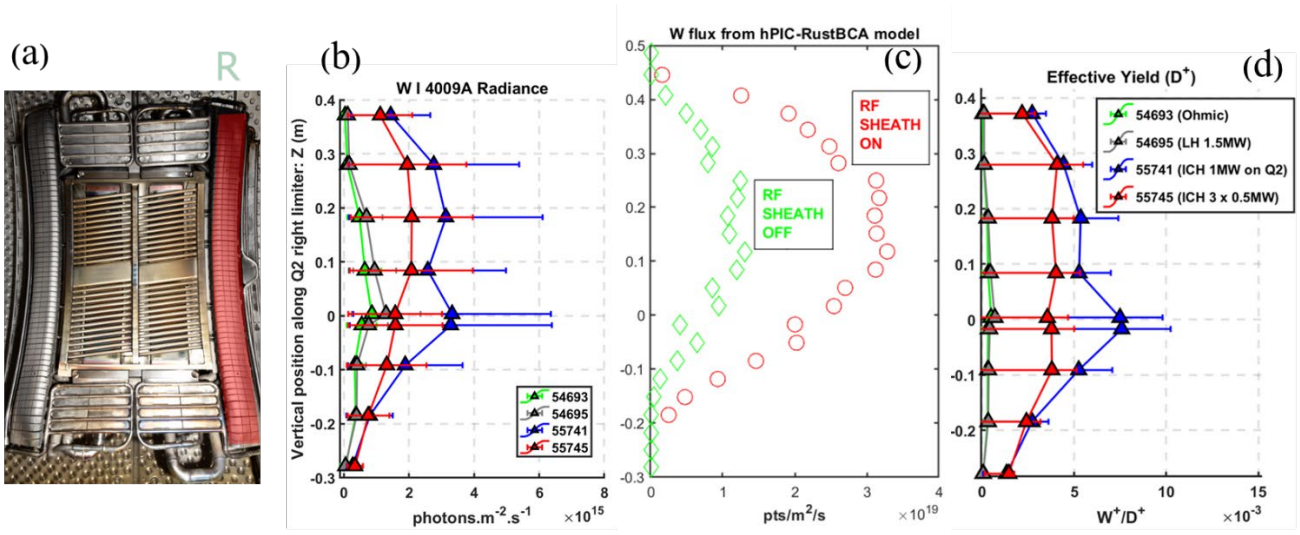

Figure 12. (a) Image of ICRH Antenna 2 with IC2R limiter highlighted; (b) measurements for ICRH-only shots, on similar target plasmas as the LH-only shots of Fig. 3, super-imposed with the latter; (c) a first simulation using hPIC-RustBCA with added RF sheath effect, specifically for the case of WEST Shot 55741, and assuming 100V peak-to-peak near-field at the observed limiter; (d) a D^+ effective yield particularly emphasizing the impact of the RF sheath on erosion for this shot with all the ICRH power applied to the observed antenna (Shot 55741).

The W^+ and D^+ fluxes used to derive the curves in Fig. 12-d are based on the spectral radiance values of Fig. 12-b. The inverse photon efficiencies (S/XB) were calculated with ColRadPy using a range for n_e from 1 – 10 x 10^{17} and taking Te to be in the 12+/-1 eV range. The error bars then in Fig. 12-d come directly from varying these parameters. The reason it was done this way is that the RCP data has an uncertainty in probe sweeping position with respect to location of the separatrix. This was contrary to the RCP data from the LH-only dedicated session, where it had been possible to validate the RCP probe profile position against a fixed probe embedded in one of the LH launchers.

The hPIC code includes an RF-sheath capability [**33**]. A first simulation using this capability is carried out here for WEST Shot 55741, in which all ICRH power (1MW total) was applied to the observed ICRH antenna (Fig. 12a). This is the same antenna, whose right-side guard limiter was used as the proxy main chamber plasma-facing surface, including for the LH-only shots, when this antenna was in passive state. The result of the simulation is shown in Fig. 12c, with the RF sheath effect turned on and off. The ~3x increase in W flux, as calculated with this rough model, is qualitatively consistent with the similar increase in W I emission indicated in Fig. 12b, seen when comparing the higher power ICRH-only shot with the average value of the LH-only shots. The zero values in the Fig. 12c simulation plot are from limiter tiles that are furthest from the separatrix, where the plasma parameters were too low for the simulation to converge. A more detailed analysis and a refined RF sheath-specific erosion modeling study are under way.

2.4 Modelling study of the sources from the divertor

Here the latest SOLEDGE-EIRENE is used for interpretive modeling of the observed trends in the divertor W source [**19**] in 2D transport mode. For charged species, the code solves multi-fluid equations obtained from the Zdhanov closure [**34**]. Neutrals, including oxygen atoms, are modelled kinetically with EIRENE. For the divertor study, the main varying parameter was P_{SEP}, and the transition from a sheath limited regime to a detached regime for a fixed density at the core edge interface (CEI) of 8x10^{19} m^{-3} at the inner computational boundary. The simulation domain is therefore technically fueled from the core to maintain this density, and a pump with an albedo 0.95 is implemented under the baffle (on the surface at Z ~ -1m and R=2.5 m on Fig. 1, which models the entrance of the pump duct). The simulations are run with O as a representative impurity (a light impurity proxy) with the same atomic data as used in Section 2.2 (from the ADAS database) and a fixed concentration of 3% at the CEI (in line with estimations in Ref. [**35**]). This choice for the oxygen source is motivated by the fact that no experimental information is available on the strength and localization of sources of oxygen at the wall. Furthermore, oxygen is meant to be a representative impurity here, and the sources of other impurities are also essentially unknow. As a final note, and as already published in Ref. [**30**], the O concentration is spatially inhomogeneous, such that the concentration imposed here for the divertor study is, in fact, compatible with a 5% concentration in front of the limiter as assumed in the previous section. The cross field transport coefficients (resp. for particle, momentum and energy) are spatially homogenous, and such that D=0.2 $m^2.s^{-1}$ for all species, ν =0.2 $m^2.s^{-1}$ and $\chi_{i,e}$ =0.6 $m^2.s^{-1}$. Note that drifts are turned off for these runs.

The sputtering yield is calculated by EIRENE using a modified Bodhansky fit formula [**36**]. SOLEDGE computes T_e, T_i and the parallel Mach number $M_{\parallel}$ at the sheath entrance. From this, EIRENE samples ions from a shifted truncated Mawxellian (centered around $M_{\parallel}c_s$ in the parallel direction). These ions are then accelerated in the direction normal to the wall with the sheath potential ~ $3ZT_e$. As a result, their mean energy is close to $2T_i$+$3ZT_e$. The angle distribution is peaked around ~ 60° with respect to the material surface for D, which is higher than what the hPIC modeling shows. However, EIRENE uses sputtering yields which depend only on energy, and the outgoing angle distribution is cosine so that the angle distribution does not matter in this model. The description of sputtering is thus much less refined than in the limiter simulation, in accordance with the more qualitative goals. Relaxing these approximations would require integrating SOLEDGE into the workflow presented in Ref. [**15**], in place of SOLPS. The W I emission is then recalculated using the S/XB values from ColRadPy and smoothed spatially (moving average of 1 cm along the wall) to emulate the sightline spot width on the targets.

As shown on Fig. 13 a) and b), target conditions show very similar electron temperatures, but the electron density at the location where the temperature peaks is significantly lower at the inner target after a transition occurs above 1.5MW. A marked asymmetry in the O concentration develops (see Fig. 13c), featuring higher fluxes/concentration in the inner leg. This is very similar to what has been observed and discussed in terms of the parallel force balance in Ref. [**30**]. Note that the mean O charge (calculated by integrating over the target profiles) remain fairly high in all cases, even at the lowest power, essentially because recombination times are much larger than parallel transit times (as was already pointed out in the discussion of Section 2.2). Comparison of ionization stages-resolved fluxes show that the asymmetry is mostly significant for O ions with charges higher than Z=5, which dominate the O fluxes at the target (as shown by the plot of the mean ion charge at the targets). This results from the

parallel force balance for impurities, and the scaling of the different forces with the ion charge (as discussed in Ref. [**37**]), and is presently the subject of more detailed investigations.

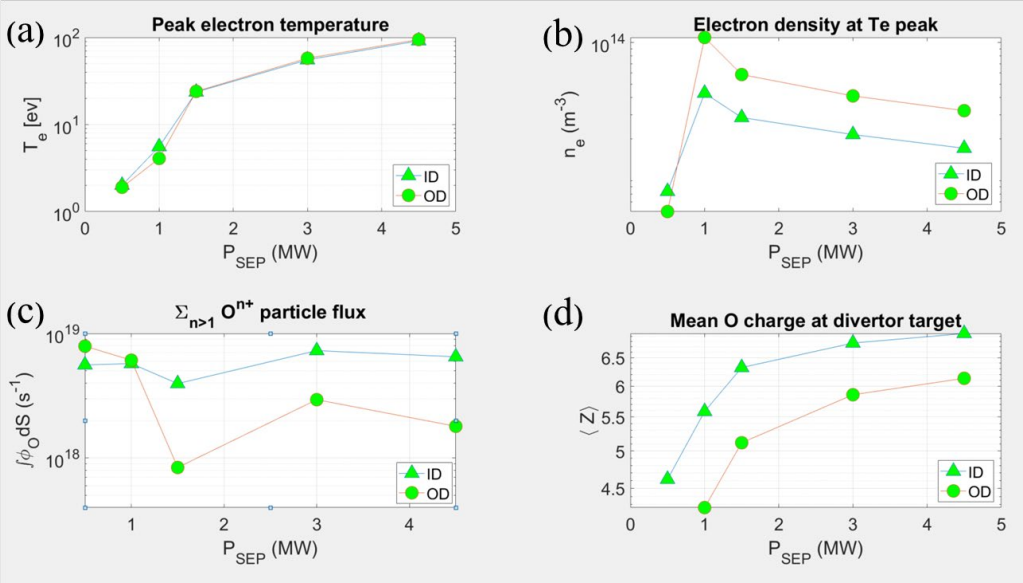

Figure 13. SOLEDGE-EIRENE simulation plots including (a) peak divertor temperatures (Inner Divertor, ID; Outer Divertor, OD) as a function of the power into the main plasma, exhibiting nearly symmetric peak T_e across the whole power range; (b) electron density at the temperature peak location; (c) oxygen flux summed over all ionization stages; (d) mean oxygen charge state, showing monotonic increase over the full power range of the study, but always >> +1.

These asymmetries lead to higher O-induced W sputtering in the inner leg, until sputtering by D begins when T_e approaches ~50 eV. This is seen in Fig. 14, where the wall coordinate is as defined in [**30**], running poloidally down from HFS midplane, across the lower divertor and back up across the LFS PFCs. At the lowest power (~0.5 MW), sputtered fluxes in the inner and outer divertor are close and fully O dominated, but the strong T_e dependence of the S/XB between 1 and 2 eV and spatial profiles along the divertor target are key factor explaining the W I peak emission asymmetry in the simulation. In fact, the W I peak emission asymmetry results from complex spatial patterns for the particle fluxes (of oxygen mainly except at the highest power), electron and ion temperature profiles along the target. The latter will define the W sputtered profile and the position of its peak. The emission profile is then calculated by multiplying by the S/XB calculated along the target using local n_e and T_e values since W I (neutral tungsten) emission is strongly localized close to the target because of mean free paths of the order of the mm. This step can distort quite significantly the sputtered flux profile because the S/XB can have a strong dependence on Te, especially at low temperature. The W I emission profile along the target is then smoothed with a length scale corresponding to the width of the sightline.

Figure 15 shows the dependence of the peak emission from the inner and outer strike regions of the divertor on P_{SEP}, both from experiments and simulations. The three shared regions, left-to-right, group the points by OH, then the low power scan, LH-only (as in Figures 3 and 4, and with target plasma based on the Ohmic) and with higher power. Further discussion of the peak emission data in this figure can be found in [**21**].

Overlayed on the Figure are simulated W I peak emission values from a SOLEDGE-EIRENE power scan over the same power range. The fairly good overlap is likely to be somewhat fortuitous, as the simulation are not tailored to match all the plasma backgrounds, and as the spectral emission has not yet fully incorporated an emerging WEST sightline synthetic diagnostic. However, the principal aim here is to illustrate the fact that a power scan, keeping all other parameters fixed, is able to not only reproduce the overall trend with increasing power crossing the separatrix, but also that the simulated changes in the divertor in-out asymmetry in the W I emission exhibit a complex behavior which reproduces qualitatively

some of the salient features of the experimental data, that is: the direction of the asymmetry and its reversal from ohmic shots to LH heated shots. However the level of asymmetry, the increase of peak emmission with power and the behavior for the extra high LH power shot is not well captured, and will need more fine tuning of the simulations, and also bringing drifts into the picture.

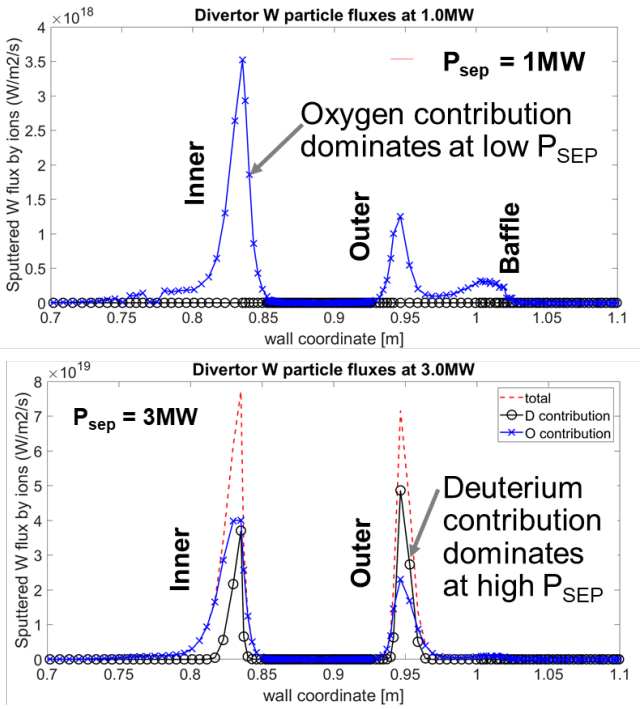

Figure 14. Simulated divertor W sputtered flux from the SOLEDGE-EIRENE power scan, showing how the in-out asymmetry in W flux could be influenced both by changes in oxygen ion flux and by an increasing role of main ion flux at the higher powers.

These encouraging results will have to be confirmed in near future measurements in dedicated experiments when the embedded divertor probe arrays become available [**38**], at the same time as full radial spectroscopic coverage of the divertor. The combination will provide key information to unambiguously identify the mechanisms explaining emission asymmetry. The results reported here clearly show that main plasma divertor imbalance is not a necessary ingredient.

It should be noted that these cases are performed without drifts. Nonetheless, the combination of changes in (i) target conditions, (ii) main plasma parallel profiles affecting impurity transport, and (iii) S/XB values, owing to their T_e and n_e dependence, already show a complex behavior and provide clues to the interpretation of the experiments.

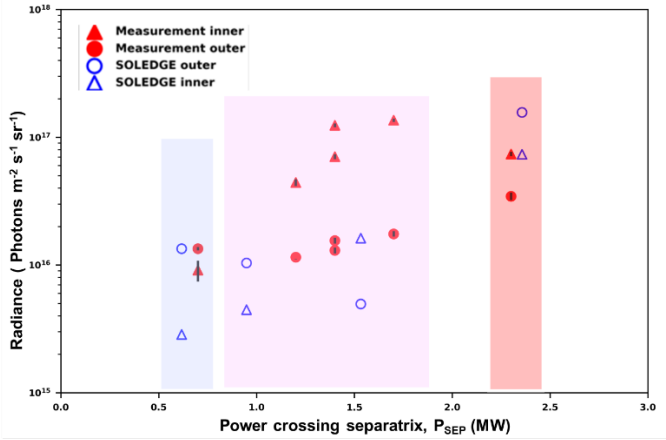

Figure 15. WEST Phase 1 experimental results with W I 4009 Å emission as proxy for gross erosion (red symbols) and with SOLEDGE-EIRENE simulated emission overlayed (blue symbols). The shaded boxes denote (left to right) Ohmic, LH power scan in dedicated experiment, extra high LH power discharge with otherwise similar parameters at the analysed time window.

3. Discussion and conclusions

In this work, we use emerging simulation tools to interpret experimental trends in W sources from the main chamber and divertor in WEST. The focus has been on the dependence of the gross sourcing from these two regions on the total power crossing the separatrix in LSN discharges, as opposed to net sources which would be the ultimate aim. The reason for focusing on gross W sourcing/erosion at this point in time, is that it provides the most direct comparison between measurements and simulation. Without further measurement constraints interpreting net sources at this scale is counterproductive, and is therefore left for future work. Nonetheless, this work has shown that although the main chamber source is significantly lower than peak divertor sources, it increases linearly with the total power mainly driven by an increase in the SOL Te.

These interpretive studies have clearly highlighted the role of light impurities, with emphasis on oxygen. In particular, it was seen that significantly high ionization stages of oxygen can dominate the W sputtering process in both divertor and limiter regions. The outcome has made clear that the emission from singly ionized oxygen (O II lines) can not be used to constrain erosion simulations excusively, as originally envisioned. Although, the low charge state emission can aid in the overall calculations for the ionization balance (e.g., by constraining local recycling effects) and is, therefore, useful measurement. Nonetheless, extending visible spectroscopy capabilities, as well as vacuum ultra-violet (VUV) for the plasma boundary

as highlighted in Ref. [**30**] is critical for acurate interpretation of the PFC erosion. Planning is on-going to deploy such capability on WEST for assessing both oxygen and for W higher ionization stages [**39**].

The outcome of the interpretive studies in this paper are encouraging in terms of the capabilities of simulation tools to aide in the interpretation of data from judiciously designed experiments using current capabilities. From the limiter study, the strong response to the simulated sputtering flux to P_{SEP} was consistent with the response of the W I line emission, thus also adding confidence to the choice of using this emission intensity as proxy for gross erosion. On the other hand, the effort to quantitatively match the simulated photon flux to the measured W I exposed sources of uncertainty, including the inverse photon efficiencies and the oxygen fractional ionization stage abundances. The near-quantitative matching of data at higher ionization states of oxygen is a notable outcome of this study.

The SOLEDGE-EIRENE simulations not only informed the processes driving the in-out asymmetry in the W I emission in the divertor, but it also reinforces the limiter study conclusion that the high ionization stages of oxygen could dominate the sputtering processes. The absence of validated data from divertor embedded probes is a notable ommission in the otherwise optimal set of shots for these studies. Nonetheless, this is filled in by the simulation, however, the simulated Te values for the higher powers are somewhat higher than expected. Up-coming experiments are planned to fill this void.

Lastly, the preliminary simulations of an ICRH-only shot showed promise in further development of this capability for interpretive modeling. The values of additional RF sheath-specific potential needed at the limiter surface to reproduce the ~x3 increase in local gross erosion is quite compatible with similar findings from JET-ILW measurements with edge beryllium line emission [**40**, **41**] and simulation using ERO [**42, 43**], as well as studies in ASDEX-Upgrade with (non-optimized configuration) antenna protection, W limiters [**44**]. More systematic analysis for the WEST ICRH vs LH comparisons are under way and additional interpretive modeling development is anticipated.

Fully accounting for the higher charge states of impurity ions requires more dedicated measurement efforts for emission of these ions. Consistent modeling is also needed. Both of these endeavors are expected to be key drivers of dedicated experiments in the upcoming WEST Phase 2 experimental campaigns.

Acknowledgements

Valuably guidance from Dr. G.M. Wallace (MIT) on handling the magnetic equilibria for the limiter model is gratefully acknowledged. This work was funded, in part, by the US Department of Energy under Contract No. DE-AC05-00OR22725 with UT-Battelle, LLC. Part of this work has been carried out within the framework of the French Research Federation for Fusion Studies**.**

References

[1] Pitts R A et al. 2019 *Nucl. Mater. Energy* **20** 100696
[2] Thoma A et al 1997 *Plasma Phys. Control. Fusion* **39** 1487
[3] van Rooij G J et al. 2013 *J Nucl Mater* **438** S42–S47
[4] Brezinsek S 2015 *J Nucl Mater* **463** 11-21
[5] Fedorczak N 2015 *J Nucl Mater* **463** 86-90
[6] Bourdelle C et al 2015 *Nucl. Fusion* **55** 063017
[7] Di Genova S et al. 2021 *Nucl. Fusion* **61** 106019
[8] Dux R et al. 2011 *Nucl. Fusion* **51** (5) 053002
[9] Marandet Y et al. 2015 *J. Nucl. Mater.* **463** 629-633; https://doi.org/10.1016/j.jnucmat.2014.11.030
[10] Stangeby P et al. *Plasma Phys Control Fusion*, **64** 055018.
[11] Meyer O et al. 2016 *Rev. Sci. Instrum*. **87** 11E309; https://doi.org/10.1063/1.4959780
[12] Meyer O et al. 2018 *Rev. Sci. Instrum.* **89** 10D105; https://doi.org/10.1063/1.5035566
[13] Salasca S 2014 *IEEE Trans. Plasma Sci.* **42** (5) 1449-1456
[14] Gunn J P and Pascal J.-Y. 2011 Rev. Sci. Instrum. **82** 123505; 10.1063/1.3661128.
[15] Wirth B D et al., IAEA-FEC'20, May 2021
[16] Khaziev R, Curreli 2018 *Computer Physics Comm*. **229** 87 doi:10.1016/j.commatsci.2018.03.032
[17] Drobny J, Curreli D, 2018 *Computational Materials Science* **149**, 15, pp. 301–306; doi: 10.1016/j.commatsci.2018.03.032
[18] Drobny J T, Curreli D, 2021 *Journal of Open Source Software* **6**, 64, 3298 :doi:10.21105/joss.03298
[19] Bufferand H et al 2021 *Nucl. Fusion* **61**(11) 116052
[20] Coenen J W et al. 2015 *J Nucl Mater* **463** 78-84
[21] Unterberg E A, Klepper C C et al. "Determining the Poloidal Distribution of W Erosion by Light Impurities & Heating Strength in WEST," from TOFE-2020 Conference and currently in process of submission to Fusion Sci & Technol
[22] R. Khaziev, D. Curreli, Physics of Plasmas, Vol. 22, Is. 4, 043503 (2015)
[23] Kallenbach A et al 2005 *Plasma Phys. Control. Fusion* **47** B207
[24] Beigman I et al 2007 *Plasma Phys. Control. Fusion* 49 1833; doi:10.1088/0741-3335/49/11/006
[25] Brezinsek S et al, 2017 *Phys. Scr.* 014052; doi:10.1088/1402-4896/aa8a45
[26] Johnson C A, Loch S D and Ennis D 2019 *Nuclear Materials and Energy* **20** 100579

[27] Johnson, C A, S D Loch, and D A Ennis. 2021 *Plasma Phys Control Fusion* **62** 125017. DOI:10.1088/1361-6587/abc08b
[28] Smyth R T et al 2018 *Physical Review A* **97** 052705; 1–9
[29] Summers H P, Dickson W J, O'Mullane M G, Badnell N R, Whiteford A D, Brooks D H, Lang J, Loch S D, and Griffin D C. 2006 *Plasma Phys Control Fusion* **48** (2) 263-293
[30] Gallo A et al 2020 *Nucl. Fusion* **60** 126048
[31] Urbanczyk G et al. 2021 NME **26** 100925
[32] Urbanczyk G et al., 2021 *Nucl. Fusion* **61** 086027
[33] Elias M, Curreli D, Myra J 2021 *Physics of Plasmas* **28** 052106
[34] Bufferand H et al. 2022, *Plasma Phys Control Fusion*, **64** 055001.
[35] van Rooij G J et al 2020 *Phys. Scr.* **2020** 014060
[36] Eckstein W, Gracia-Rosales C, Roth J, Ottenberger W, 1993 IPP Report 9/82, Table 3, page 335
[37] Senichenkov Y et al. 2019 *Plasma Phys. Control. Fusion* **61** 045013.
[38] Grosjean A et al., "Development of an integrated multi-diagnostic to assess the high-Z impurity fluxes in the metallic environment of WEST using IMAS" IEEE *Transactions on Plasma Science*, In Print (DOI: 10.1109/TPS.2022.3187619)
[39] Guirlet R et al 2019 J. Instrum. **14** C10036
[40] Klepper C C et al. 2013 *J. Nucl. Mater.* **438** S594–S598
[41] Bobkov Vl et al. 2013 *J. Nucl. Mater.* **438** S160–S165
[42] Klepper C C et al 2016 *Phys. Scr.* **2016** 014035
[43] Lasa A et al 2018 *Nucl. Fusion* **58** 016046
[44] Bobkov Vl V et al 2010 *Nucl. Fusion* **50** 035004